# Biophysical characterization of collimated and uncollimated fields in pencil beam scanning proton therapy


## Abstract

**Objective:** The lateral dose fall-off in proton pencil beam scanning (PBS) technique remains the preferred choice for sparing adjacent organs at risk as opposed to the distal edge due to the proton range uncertainties and potentially high relative biological effectiveness. However, because of the substantial spot size along with the scattering in the air and in the patient, the lateral penumbra in PBS can be degraded. Combining PBS with an aperture can result in a sharper dose fall-off, particularly for shallow targets. **Approach**: The aim of this work was to characterize the radiation fields produced by collimated and uncollimated 100 and 140 MeV proton beams, using Monte Carlo simulations and measurements with a MiniPIX-Timepix detector. The dose and the linear energy transfer (LET) were then coupled with published *in silico* biophysical models to elucidate the potential biological effects of collimated and uncollimated fields. **Main results**: Combining an aperture with PBS reduced the absorbed dose in the lateral fall-off and out-of-field by 60%. However, the results also showed that the absolute frequency-averaged LET ($LET_F$) values increased by a maximum of 3.5 keV/µm in collimated relative to uncollimated fields, while the dose-averaged LET ($LET_D$) increased by a maximum of 7 keV/µm. Despite the higher LET values produced by collimated fields, the predicted DNA damage yields remained lower, owing to the large dose reduction. **Significance**: This work demonstrated the dosimetric advantages of combining aperture with PBS coupled with lower DNA damage induction. A methodology for calculating dose in water derived from measurements with a silicon-based detector was also presented. This work is the first to demonstrate experimentally the increase in LET caused by combining PBS with apertures, and to assess the potential DNA damage which is the initial step in the cascade of events leading to the majority of radiation-induced effects.

# 1. Introduction

The proton PBS technique enables the delivery of highly conformal dose distributions while minimizing the dose to healthy tissues (Durante and Paganetti 2016). In addition to the clear dosimetric advantages over conventional photon radiotherapy for many treatment sites, PBS also reduces the overall neutron dose compared to proton passive scattering delivery systems (Schneider *et al* 2002). However, due to the inherent range uncertainties in proton beams and the higher relative biological effectiveness (RBE) at the distal edge (Paganetti *et al* 2002, Knopf and Lomax 2013, Lühr *et al* 2018, Paganetti *et al* 2019, Tattenberg *et al* 2022), the lateral edge is typically used for sparing critical organs. Therefore, reducing the width of the lateral penumbra is essential in order to minimize the dose to the adjacent organs at risk (OAR). Although PBS generally offers a superior dose conformity, the substantial spot size and the scattering in the air result in a larger lateral penumbra in the patient compared to collimated broad divergent beams (Safai *et al* 2008). This effect was shown to be mostly pronounced at shallow depths and large air gaps (Safai *et al* 2008, Maes *et al* 2019).

The lateral dose fall-off in PBS with and without collimation and the clinical implementation of collimation systems were investigated in many studies. Winterhalter *et al* compared different penumbra enhancement scenarios with various pre-absorber strategies in order to optimize the lateral dose fall-off (Winterhalter *et al* 2018). Maes *et al* experimentally validated the treatment planning system (TPS) Monte Carlo (MC) dose calculation of the lateral penumbra in collimated PBS for different parameters such as depth, air gap and range shifter thickness. In the same study, the authors characterized the reduction of the lateral penumbra between collimated and uncollimated PBS for varying values of these parameters (Maes *et al* 2019).

Collimation was shown to be particularly advantageous when range shifters are used. This was demonstrated through MC simulations for the development of collimator designs and the implementation of MC calculations in planning systems (Charlwood *et al* 2016). Bäumer *et al* showed that placing the aperture downstream of the range shifting block reduced the width of the lateral penumbra by 20% compared to placing the aperture upstream (Bäumer *et al* 2018). Moreover, the clinical implementation of static field-specific apertures presented dosimetric

advantages, particularly for sparing nearby OAR while also improving the conformity index by 10-20% (Bäumer *et al* 2021).

Dynamic collimation systems (DCS) have also gained importance over the past few years given their inherent flexibility, which enables the collimation of multiple energy layers. This was demonstrated in (Hyer *et al* 2014) by using two pairs of motorized parallel nickel trimmers to reduce the lateral penumbra with a small footprint and a cost-effective design. The use of DCS with PBS was also shown to improve the dose distribution and normal tissue sparing in the treatment of head and neck cancers (Moignier *et al* 2015). More recently, a Monte Carlo package for modeling DCS was developed which included a generalized PBS source model, trimmers and range shifters, intended to be used for future treatment planning and dosimetry (Nelson *et al* 2021). Although no patients were involved in these studies, the Mevion PBS system (Mevion Medical Systems Inc., Littleton, MA, USA) which features the fully automated Adaptive Aperture™ is used clinically. All these studies point towards the fact that collimation systems in combination with PBS lead to superior dose distributions, which will pave the way towards standard clinical implementation. However, the overall biological impact of combining apertures with PBS remains unclear and should be carefully considered for optimizing treatment plans.

The biological impact of collimator-scattered protons was investigated in (Ueno *et al* 2019) using biophysical modeling. The authors found an increase in the dose-averaged LET ($LET_D$) associated with collimator-scattered protons using MC simulations but the increase in RBE was negligible. Nevertheless, these results were not compared to uncollimated fields. Moreover, the choice of the RBE model is crucial and clonogenic cell survival may not be a relevant endpoint for normal tissue response (Paganetti *et al* 2019). On the other hand, DNA damage is considered the initial event that triggers the majority of radiation-induced effects. DNA double strand breaks (DSBs) are known to be the most harmful lesions. As the LET increases, the density of ionization events also increases, resulting in a higher number of potentially clustered and more complex DSBs (Vitti and Parsons 2019). This can further translate into lethal residual breaks and an increase in chromosomal aberrations, which can be mutagenic or lethal. For these reasons, using biophysical models that allow to predict the DNA damage would be more relevant to estimate the biological effect of the collimation.

In this work, we investigate the impact of combining PBS with a brass aperture on the absorbed dose and LET distribution in water using measurements and simulations. The absorbed dose and LET are then used to elucidate the biological effects, particularly the difference in the potential DNA damage induced by collimated and uncollimated fields using published *in silico* biophysical models.

# 2. Materials and Methods

## 2.1. Experimental set-up

Measurements were performed at the West German Proton Therapy Centre Essen (WPE). A MiniPIX-Timepix detector was placed inside a waterproof PMMA holder. The latter was similar to the one used in (Stasica *et al* 2020). However, it was adapted such that it could be attached to the positioning system suitable for the horizontal irradiation of this work. The detector was mounted on the Zaber XYZ motorized linear stages, which enabled remote positioning along the three dimensions[1] and immersed in the PTW water phantom (type 41023) for a horizontal beam[2].

The irradiated fields consisted of single energy layers of 100 or 140 MeV proton kinetic energy. All the fields were delivered with the IBA universal nozzle inside the fixed-beam treatment room of the WPE. The uncollimated fields were delivered in a rectangular pattern of 40 x 40 spots with a 2.5 mm spot spacing. As for the collimated fields, a brass aperture with a rectangular opening of 8.9 x 8.7 $cm^2$ was mounted in the IBA universal nozzle (Bäumer *et al* 2021). The collimated plans included an extra rim resulting in 41 x 41 spots. Both fields produced the same field-size (10 x 10 $cm^2$) at the isocenter, located at the center of the 30 x 30 x 30 $cm^3$ water phantom. The TPS RayStation (RaySearch Laboratories, Stockholm, Sweden) Research 7 was used to create the plans. More details on the proton field delivery can be found in (Bäumer *et al* 2017, 2018, 2021).

[1] https://www.zaber.com induction
[2] https://www.ptwdosimetry.com/

## 2.2. MiniPIX-Timepix detector

The MiniPIX-Timepix detector, developed by ADVACAM[3] and used in this study, is a semiconductor pixel detector equipped with a 500 µm thick silicon sensor. The latter is bump-bonded to a high-granularity Timepix application-specific integrated circuit (ASIC) chip consisting of 256 x 256 pixels with independent readout chains and a total sensitive area of 1.4 x 1.4 $cm^2$. The detector can be used for a wide range of spectral and directional sensitive characterizations of mixed radiation fields, while enabling visualization of single particle tracks.

When a particle deposits energy in the sensor, a large number of electron-hole pairs are generated. During the charge collection process in the semiconductor, the charge carriers will drift towards the corresponding electrode under the influence of the applied bias voltage, and will spread laterally due to diffusion, creating the so-called charge sharing effect. As a result, the signal is spread to nearby pixels forming a pixel cluster (Campbell *et al* 2008, Granja *et al* 2013). A detailed analysis of the pixel clusters created by each particle enables an enhanced resolving power of particle-event type (Granja *et al* 2018a).

The detector was connected via USB cable to a PC and operated using the PIXET program developed by ADVACAM. All the pixels were set to time-over-threshold, also referred to as energy mode (Llopart *et al* 2007). Measurements were performed at a bias of 80 V, which resulted in a nearly fully depleted sensor with an enhanced charge sharing effect to avoid high energy saturation in the pixels (Campbell *et al* 2008, Granja *et al* 2011). In order to limit the overlap of events and enable single particle tracking, the frame acquisition time was set to 1 ms, which is the lowest value. The detector was positioned along two lateral distances, namely 7.8 and 9.3 cm from the central axis, and at various depths in water. A total of 47 measurements were performed, and an average dose of 7 Gy was delivered at 3 cm depth in water. The number of

[3] https://advacam.com

registered events in the detector ranged between $10^4$ and $10^5$. **Figure 1** shows the experimental set-up positioned in front of the IBA universal nozzle inside the fixed-beam treatment room.

Data analysis consisted of a pre-processing step using the Data Processing Engine (DPE, version 1.0.5), which is a tool with an embedded database used for processing the data acquired with Timepix detectors (Marek *et al* 2023). The output of the DPE is a list of pixel clusters, each characterized by a wide range of spectrometric and morphological parameters (e.g. event hit time, deposited energy, cluster size, roundness, linearity, 2D track length, etc.). Details on the cluster parameters have been published elsewhere (Granja *et al* 2018a). Moreover, the DPE also includes a particle identification feature. For each event, a particle classification is done according to the following three classes: 1- photons and electrons; 2- protons; and 3- heavier ions. The post-processing and calculation of dosimetric quantities are explained in the next section.

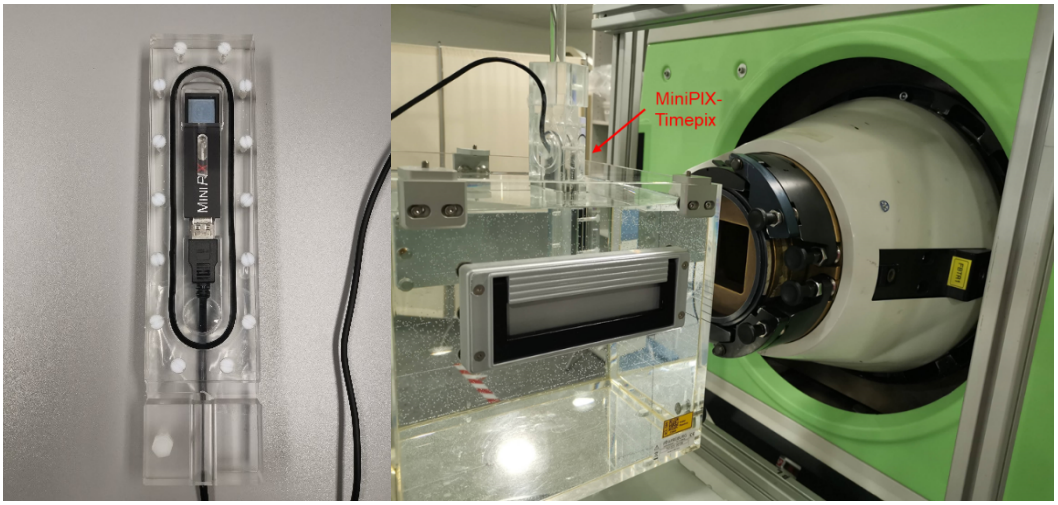


**Figure 1.** MiniPIX-Timepix enclosed in the waterproof PMMA holder (left) and placed inside the water phantom in front of the IBA universal nozzle in the fixed-beam treatment room of the West German Proton Therapy Centre Essen (right).

## 2.3. Dose calculation

Using the cluster lists generated by the DPE, the absorbed dose in silicon can be calculated as:

$$D = \frac{\sum_{i=1}^{N}(1.6 \text{ x } 10^{-16} \text{ x } dE_i)}{M} \quad (1)$$

Where D is the absorbed dose in silicon (Gy), $dE_i$ is the deposited energy of cluster event i (keV), and M is the mass of the active volume in the sensor (kg). Since silicon is not tissue equivalent, the dose measured by the Timepix detector was converted into dose in water. The conversion was based on the particle type.

In the case of photons, the conversion was performed for each cluster by multiplying with the ratio of mass energy absorption coefficients of water to silicon, obtained from NIST tables (Hubbell and Seltzer 1996). In the case of charged particles (class 2 and 3), the absorbed dose in silicon was multiplied by the mass stopping power ratio of water to silicon. The calculation and conversion of LET are explained in detail in the next section.

Since the Timepix exhibits a frame read-out time around 22 ms, a dead-time correction was applied to recover the lost signal. To overcome this intrinsic limitation, the deposited energy was interpolated between different frames using the nearest neighbor method. This step is also important for comparing the measured and simulated absorbed doses. Finally, the absorbed doses measured in each position were normalized to the absorbed dose in the center of the field at a depth of 3 cm in water, chosen as a reference because of the low dose gradient.

### 2.4. LET calculation

Using the deposited energy in each cluster dE (keV) and the track length across the sensor L (µm), the LET (keV/µm) for each cluster was calculated using:

$$LET = \frac{dE}{L} \tag{2}$$

The quantities L and LET were calculated using the method developed in (Nabha *et al* 2022). The method is based on the underlying assumption that the protons are crossing the entire sensor thickness. In this work, this method was extended in order to avoid underestimation of the LET for protons stopping in the sensor, which could be found at lateral positions close and distal to the Bragg peak depth. This was a two-step process.

a) First, a lookup table was created based on the proton stopping power and range tables (PSTAR program, Berger *et al* 2005) and included protons of incident energies ($E_{in}$) from 1 keV up to 200

MeV along with their corresponding range in silicon ($R_{in}$) and electronic stopping power ($S_{el}$). Then for a discrete set of incident angles between 0° (perpendicular to the plane of the sensor) and 90° (grazing the surface of the sensor), the geometrical track length L (mm) was calculated using:

$$L = \frac{t_s}{cos\ (\beta)} \tag{3}$$

where $t_s$ is the sensor thickness (mm) and β is the incident angle (°). For each pair of incident energy and angle, the residual range $R_{out}$ was evaluated:

$$R_{out} = R_{in} - L \tag{4}$$

If $R_{out}$ is negative, the deposited energy (dE) was considered to be the same as the incident energy. However, if $R_{out}$ is positive, then the energy $E_{out}$ corresponding to $R_{out}$ in the lookup table was used to calculate the deposited energy dE as follows:

$$dE = E_{in} - E_{out} \tag{5}$$

The aforementioned lookup table, which contained all the combinations of incident energies, angles and deposited energies, was then used to estimate whether or not the proton was stopping in the sensor and to estimate the corresponding LET.

b) In the second step, using the measured deposited energy and incident angle, the goal was to find the proton's incident energy which could deposit the measured energy in the sensor $dE_{meas}$ at the detected incident angle $\beta_{meas}$. The relationship between the incident energy and deposited energy at the same incident angle was found to be non-univocal, i.e. two possible incident energies could result in the same deposited energy for the same incident angle, where one corresponds to a stopper (protons stopping in the sensor) and the other corresponds to a crosser (protons crossing the entire sensor). Therefore, an iterative assessment was performed in which a comparison was made between the measured projected track length ($L_{2D}$), L calculated using eq. (3) and the two possible ranges in silicon $R_1$ and $R_2$ corresponding to the stopping and crossing

protons respectively. Considering the fact that the true range of the proton cannot be shorter than $L_{2D}$, the LET for each event was calculated either using equations (2) and (3) in the case of crossers, or using the electronic stopping power in silicon in the case of stoppers. A schematic illustration of particle crossing and stopping in the sensitive volume can be found in **Supp fig. *1***

For class 3 events (heavier ions), their LET was only used to convert the dose in silicon to dose in water. Therefore, we adopted a simplified approach in which LET in silicon was calculated using equation (2).

To convert the measured LET from silicon to water, we adopted the method of (Parisi *et al* 2022) in which a bin-to-bin conversion of LET in silicon was performed based on the ratio of electronic stopping powers in water to silicon. Since it was shown by the authors that PSTAR provided superior results compared to other databases and conversion methods, it was also used in this work to create lookup tables that relate the energy-dependent electronic stopping power of protons in silicon and water. The ratio of these values was then related to the LET in silicon and used as conversion factors. This method was directly applied to protons. For class 3 events, the approach of (Parisi *et al* 2022) was adapted to alpha particles using the alpha stopping power and range tables (ASTAR program, Berger *et al* 2005) to estimate the ratio of electronic stopping power of water to silicon. Finally, the frequency-averaged LET ($LET_F$) of protons in silicon and in water was calculated using:

$$LET_F = \frac{\sum_1^n \phi_i \, x \, LET_i}{\sum_1^n \phi_i} \qquad (6)$$

where n is the number of bins in the LET spectrum, $LET_i$ and $\phi_i$ are the LET and frequency values in the $i^{th}$ bin, respectively (Granville and Sawakuchi 2015).

## 2.5. Simulation framework

Monte Carlo simulations were performed using TOPAS version 3.7 (Perl *et al* 2012, Faddegon *et al* 2020). The geometry consisted of a 30 x 30 x 30 $cm^3$ water phantom with 1 cm thick PMMA walls and a brass aperture with an opening of 8.9 x 8.7 $cm^2$. The sources were designed to

reproduce the commissioned beam, namely the depth dose curves of the lowest and highest available energies. In this work, proton beams of 100 and 140 MeV were used.

The proton pencil beams were fully characterized using the Fermi–Eyges parameters from the beam model implemented in RayStation described in (Verbeek *et al* 2021). Simulated depth dose curves were validated using the plane parallel Bragg peak chamber (PTW, Freiburg, Germany) discussed in (Bäumer *et al* 2015). Details on the beam model can be found in *(De Saint-Hubert et al* 2022). The scanned fields were sampled using the time step feature of TOPAS, by delivering 1600 spots (without aperture) and 1681 spots (with aperture), which were arranged symmetrically around the isocenter with the same spot spacing of 2.5 mm. The sources were designed to sample particles on the upstream side of the aperture and 10 cm away from the surface of the water phantom.

The default production cut of 0.05 mm for all particles and the default modular physics list implemented in TOPAS were used in all the simulations. The list includes the following modules which are based on Geant4 physics models: "g4em-standard_opt4" "g4h-phy_QGSP_BIC_HP" "g4decay" "g4ion-binarycascade" "g4h-elastic_HP" and "g4stopping"[4]. In each run, $10^6$ protons per spot were launched. This resulted in a total of 1.681 x $10^9$ and 1.6 x $10^9$ histories in the cases of collimated and uncollimated fields, respectively.

[4] https://topas.readthedocs.io/en/latest/parameters/defaults.html#parameters-default-physics

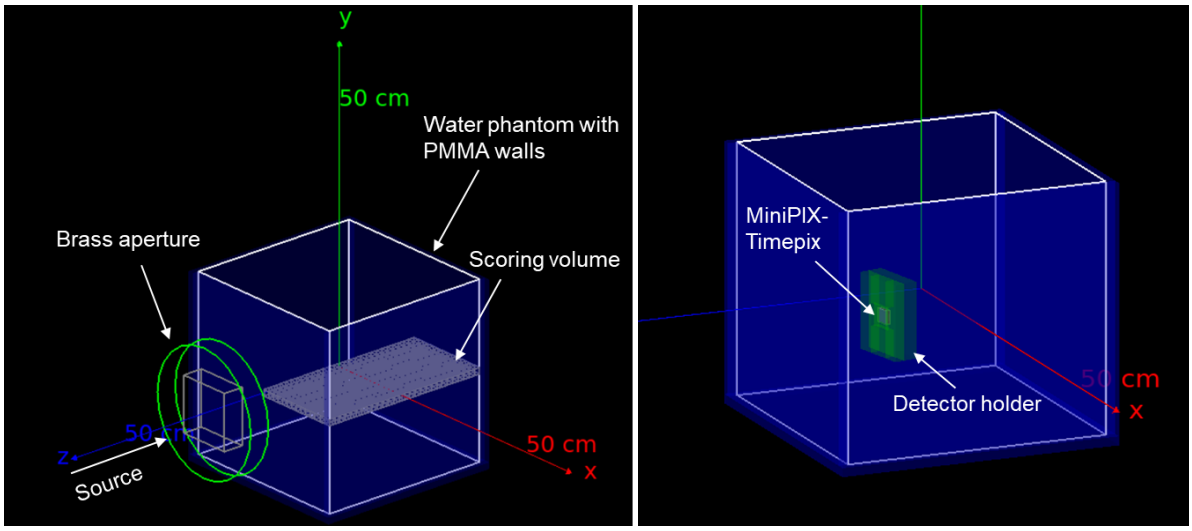


**Figure 2.** Simulation setup in TOPAS including the water phantom, aperture and scoring volume (left) and the MiniPIX-Timepix detector geometry encapsulated in the PMMA waterproof holder and placed inside the water phantom (right).

Two different scoring volumes were considered. The first one consisted of a simple scoring in the water phantom in 2 x 2 x 2 $cm^3$ voxels. This was used for scoring absorbed dose, proton $LET_D$ and $LET_F$. A voxel-wise calculation was performed to estimate the dose reduction for collimated fields relative to the uncollimated ones using the following:

$$Dose\ reduction_i = 100 \text{ x } \frac{D_{i_{uncoll}} - D_{i_{coll}}}{D_{i_{uncoll}}} \tag{7}$$

where $D_{i_{uncoll}}$ and $D_{i_{coll}}$ are the absorbed doses scored in voxel *i* with coordinates ($x_i$, $y_i$, $z_i$), for the uncollimated and collimated fields, respectively. Likewise, a voxel-wise calculation of the absolute differences in $LET_F$ and $LET_D$ for the two scenarios was carried out. On the other hand, for a precise comparison of the measured and simulated $LET_F$ values, the full detector geometry was included in the simulation setup in addition to the PMMA holder. The detector was placed at the same positions inside the water phantom as in the experiment, and the $LET_F$ was scored in the sensitive volume. The detector geometry used in the simulations was described elsewhere (Nabha *et al* 2022). Average $LET_F$ values were scored in silicon and in water by simply replacing the sensor material. **Figure 2** shows the simulation set-up including the two scoring scenarios.

## 2.6. DNA damage calculation

To assess the biological impact of using an aperture in conjunction with PBS, two LET-based models derived from track-structure simulations were used to predict the radiation-induced DNA damage. In the first approach, the analytical formulas developed by Kundrát *et al* (2020) were used, which are based on PARTRAC track-structure simulations to estimate the yields of single and double-strand breaks (DSB), clusters and sites of isolated DSBs for ions ranging from hydrogen to neon. In this work, we calculated the LET-dependent yields ($Gy^{-1}$ $GBp^{-1}$) of DSB and DSB sites using their analytical formulas and LET values calculated using TOPAS:

$$Yield = (p_1 + (p_2 LET\ )^{p_3})/(1 + (p_4 LET)^{p_5}) \quad (8)$$

The parameters $p_{i\ (i=1..5)}$, determined by the authors and corresponding to protons, were considered for the prediction of the total DNA damage yield, i.e. combining both direct and indirect damage. Moreover, the parameters $p_4$ and $p_5$ which reflect the overkill effect were omitted in the case of protons as suggested by the authors due to the absence of this effect (Kundrát *et al* 2020). The results were also multiplied by the absorbed dose in each voxel and assuming a genome of 6 GBp.

The second *in silico* model used in this work was developed in Henthorn *et al* (2019) based on Geant4-DNA track-structure simulations. A polynomial fit was applied to the average yield of DNA damage type, assuming a genome of 6 GBp, across the range of proton track-averaged LET ($LET_t$).

$$Yield\ (D, LET_t) = D\ (aLET_t{}^2 + bLET_t + c) \quad (9)$$

where D is the absorbed dose in Gy and $LET_t$ in keV/µm. Here we used the parameters for predicting simple and complex DSB. The authors defined simple DSB as breaks separated by less than 10 Bp, while the complex DSBs involve breaks with multiple associated damaged backbones (Henthorn *et al* 2019). The model was applied to the present work using the scored dose and $LET_F$ in each voxel, assuming as well a genome of 6 GBp. After applying each model to the uncollimated and collimated fields, the residual DNA damage was computed.

# 3. Results

## 3.1. Simulated dose distributions

The lateral dose profiles calculated by RayStation and TOPAS at depths of 1, 3 and 5 cm in water are shown in

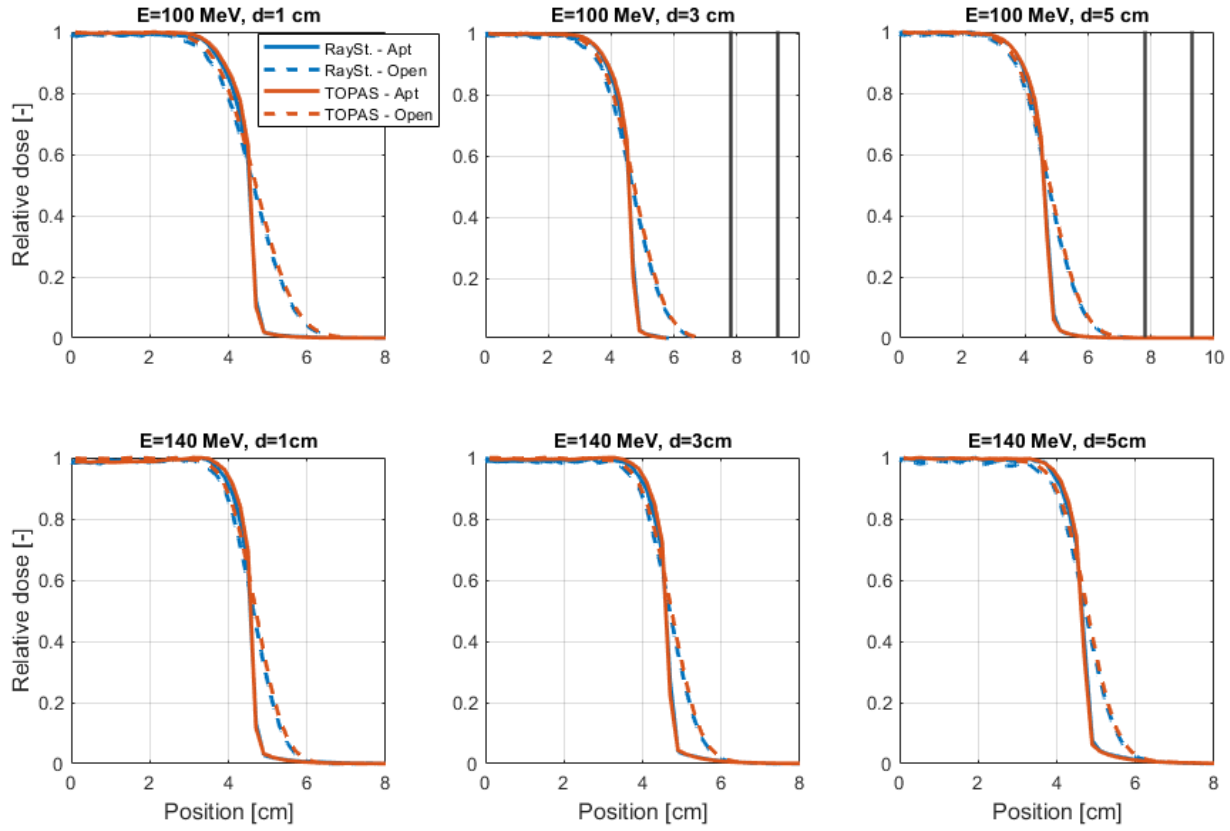


**Figure *3***. An agreement within 1% and 4% was found for the FWHM (full-width-at-half-maximum) and the penumbra width (distance between the 80% and 20% dose level), respectively. Both RayStation and TOPAS showed a sharper dose fall-off at the three depths and an average penumbra width reduction of 57% in comparison with the uncollimated fields. The simulated dose distributions in the x-z plane at 100 and 140 MeV are displayed in **Figure 4**. For each beam energy, the percentage dose reduction was calculated relative to the uncollimated fields. Simulations showed a reduction of up to 60% at the lateral field edges.

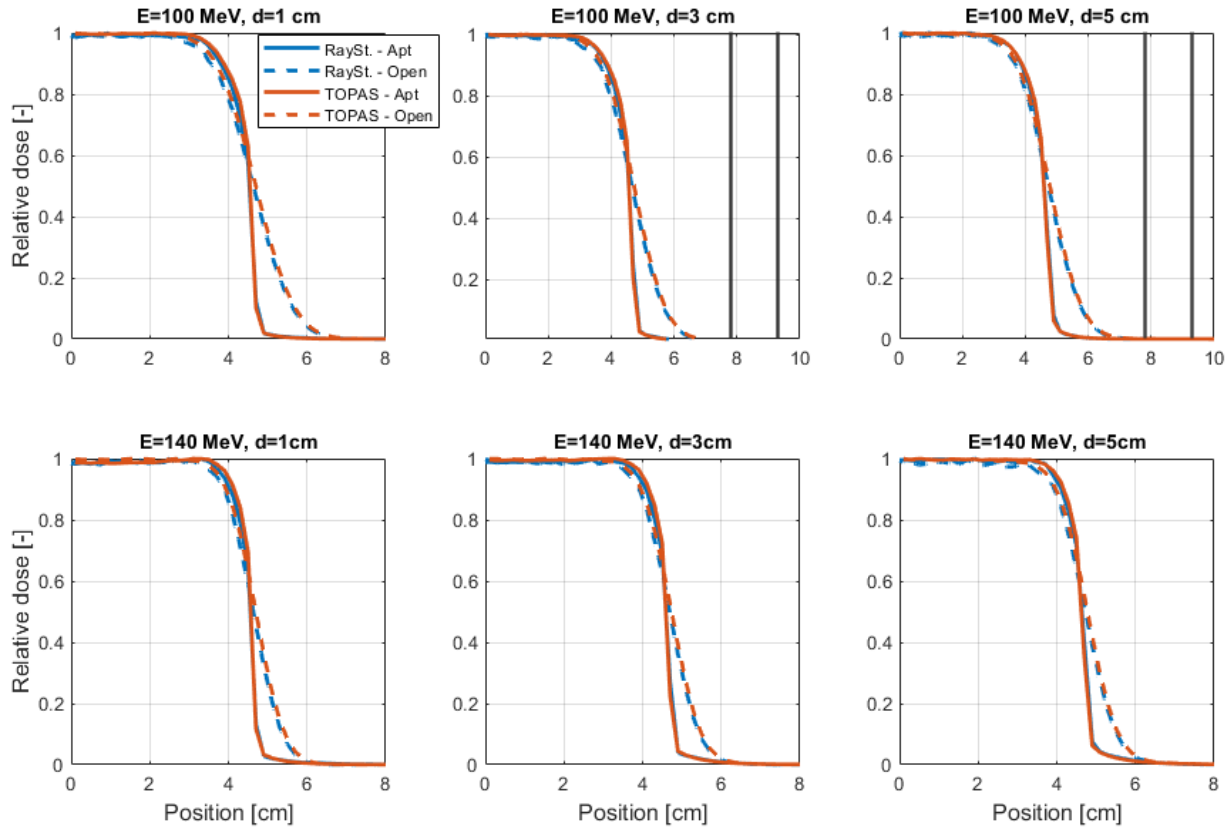


**Figure 3.** Lateral dose profiles calculated by RayStation and TOPAS at 1, 3 and 5 cm depths in water for 100 MeV (top) and 140 MeV (bottom) for open (dashed lines) and aperture-collimated fields (solid lines). The vertical lines represent the positions in which the detector was placed.

The reduction at 100 MeV was found to be nearly uniform across the depth and lateral distances, whereas at 140 MeV, there was a decrease in the dose reduction at larger lateral distances. More specifically, the dose reduction at 100 MeV spanned a region of 3 cm while at 140 MeV, this effect was observed across a wider region of 4.4 cm lateral to the field edge.

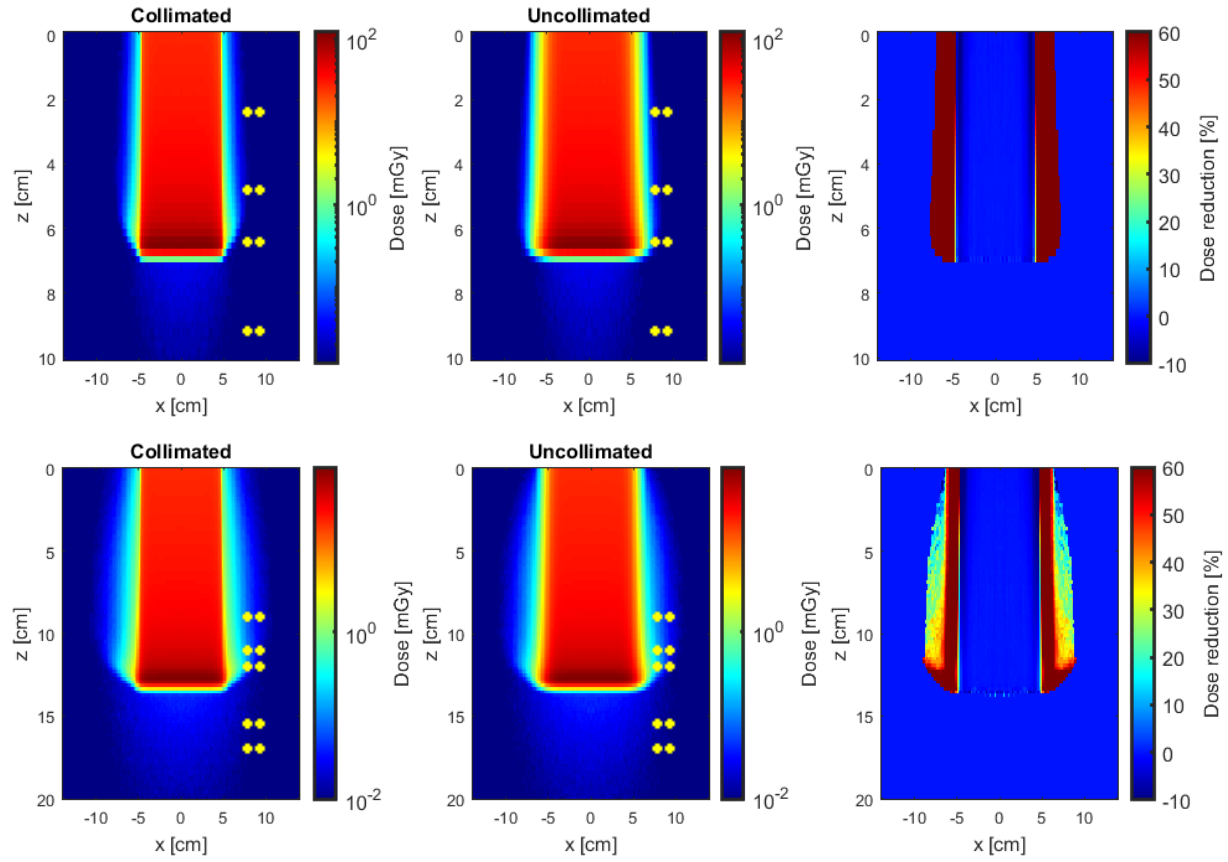


**Figure 4.** Simulated 2-D dose distribution of collimated, uncollimated fields and percentage dose reduction with respect to uncollimated fields for 100 MeV (top) and 140 MeV (bottom). The dose values displayed are shown only for voxels in which the dose was higher than 0.1% of the maximum dose. Yellow crosses represent measurement positions with the MiniPIX-Timepix detector.

## 3.2. Experimental results

The deposited energy spectra in the sensor for all events and for separate groups of events are shown in **Figure 5**. The distributions correspond to measurements at 7.8 cm from the center of the field and 6.4 cm depth in water for the collimated and uncollimated fields. In the case of the uncollimated field, the deposited energy spectra by protons featured two prominent peaks at 1.9 and 3.9 MeV. Conversely, a broad energy distribution of protons in the collimated field was observed with a smaller peak around 2.8 MeV. On the other hand, three different peaks were seen for photons and electrons in both scenarios. However, the deposited energy peaks centered around 182 and 200 keV, were 1.7 times higher in the collimated field compared to the uncollimated one. Heavier ions were virtually unaffected by the collimation.

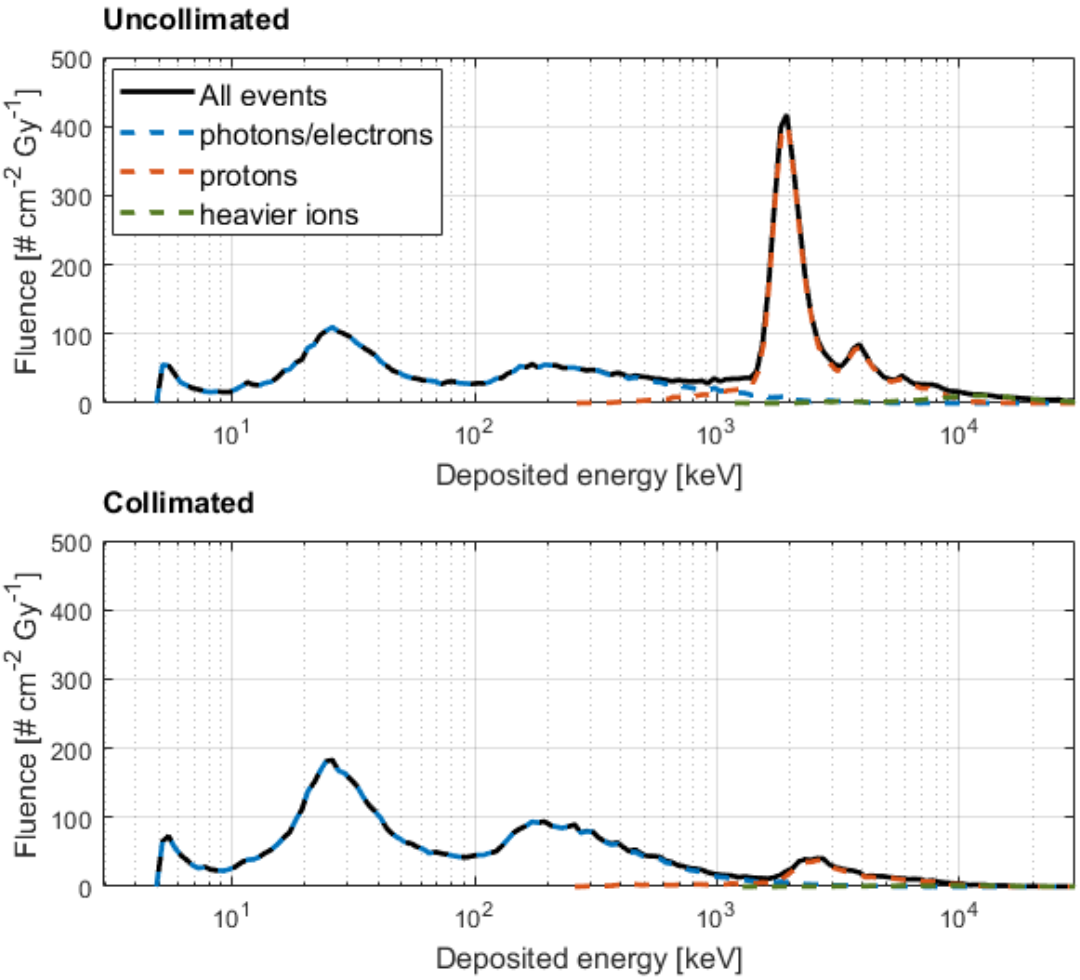


**Figure 5.** Measured deposited energy distribution in silicon for uncollimated (top) and collimated (bottom) 100 MeV proton beams, at 7.8 cm from the central axis and 6.4 cm depth. The contributions of photons/electrons, protons and heavier ions are shown in dashed blue, orange and green lines, respectively.

To gain further insight into the impact of the aperture, the angular distribution of protons measured by the detector was also evaluated. **Figure 6** shows the incident angular distribution at 100 MeV, 7.8 cm from the central axis and 2.4 cm depth in water. Both collimated and uncollimated scenarios featured broad angular distributions, which was expected given the position of the detector (i.e. outside of the primary target) and the likelihood of scattering events in that region. Nevertheless, the angular distribution of registered protons in the uncollimated

fields showed a peak around 15°, while in the collimated fields, a peak at around 40° and a smaller peak around 70° were observed.

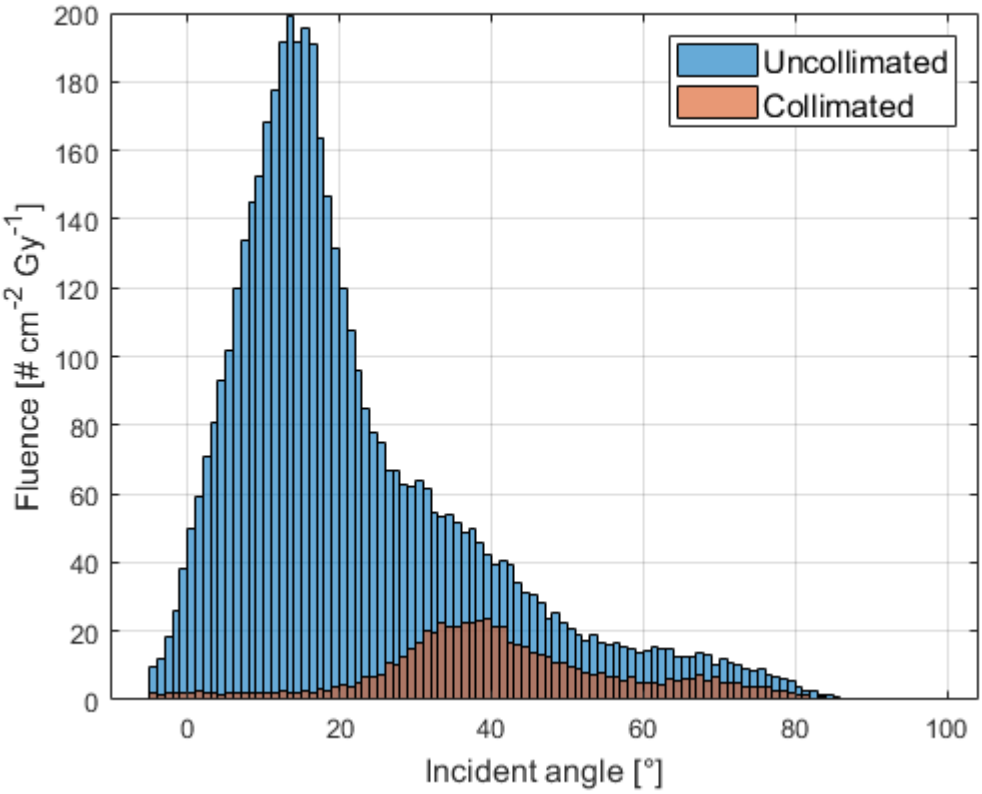


**Figure 6.** Measured angular distribution of protons for collimated (orange) and uncollimated (blue) fields at 100 MeV, 7.8 cm from the central axis and 2.4 cm depth.

The measured and simulated absorbed doses at the same lateral positions in the water phantom are shown in **Figure 7**.

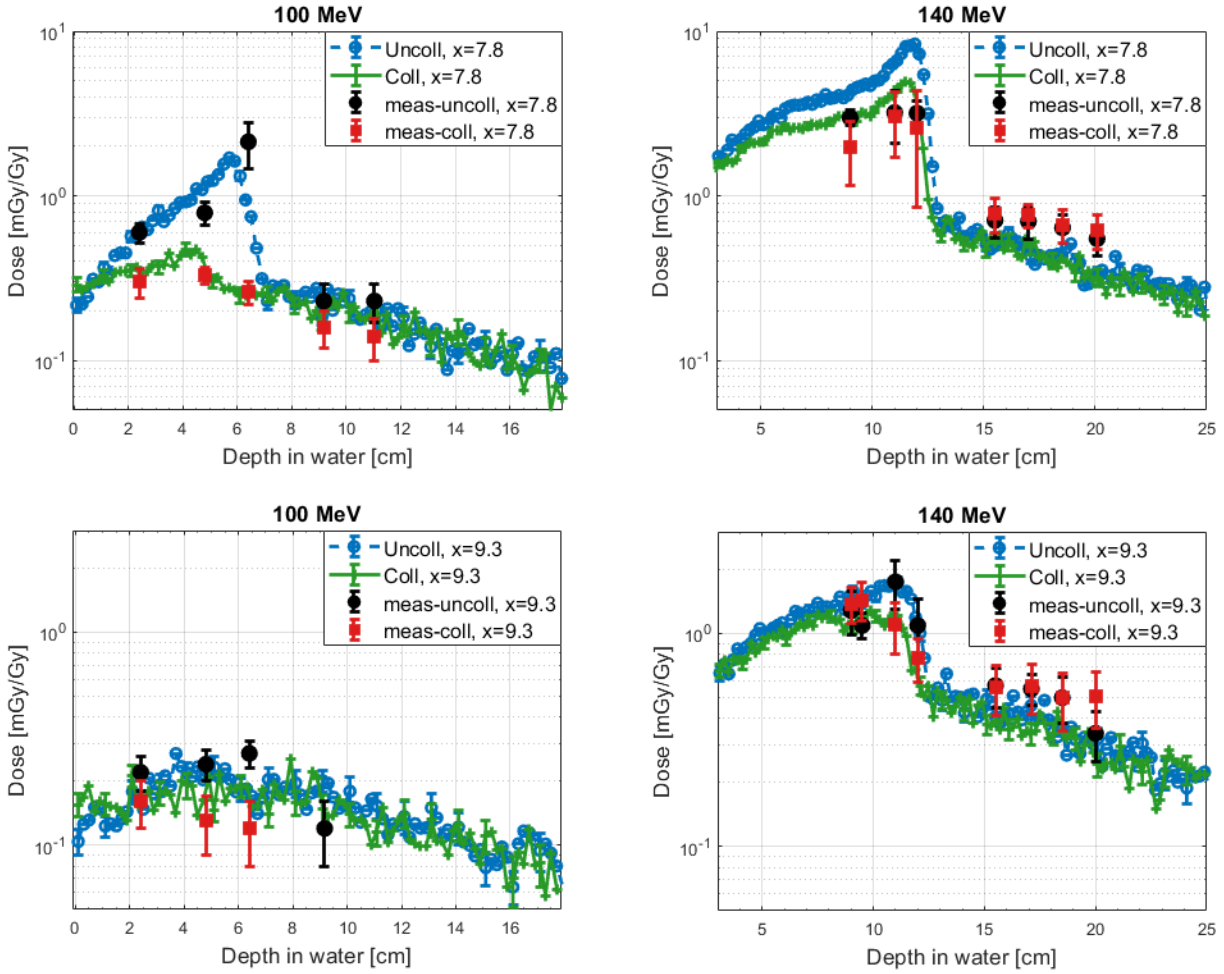


**Figure 7.** Measured and simulated absorbed dose in water at two lateral positions (x) in the water phantom and several depths. The doses are shown for collimated and uncollimated fields at 100 MeV (left) and 140 MeV (right) and normalized to the absorbed dose in the center of field at 3 cm depth.

Both measurements and simulations showed similar trends. At 7.8 cm from the central axis, an average of 65% of dose reduction was observed at 100 MeV for collimated fields in the entrance region and proximal to the Bragg peak. This effect was less pronounced at 140 MeV, for which no significant dose reduction was observed in the measurements, while simulations showed a 38 % decrease relative to uncollimated fields. Both measurements and simulations presented no collimation impact at 9.3 cm for both energies.

### 3.3. Measured and simulated LET

$LET_F$ was calculated in silicon and converted to $LET_F$ in water. The results obtained were compared to simulations that included the detector and holder geometries. $LET_F$ was scored in the silicon sensitive volume, which was then replaced by water. The measured and simulated $LET_F$ in the sensor at 7.8 cm from the center of the field are shown in **Figure 8**. An agreement within 9% and 14% was found in silicon and water, respectively. The results showed that $LET_F$ was higher in the entrance region and proximal to the Bragg peak for collimated fields relative to the uncollimated ones. Maximum absolute differences of 1.4 keV/µm and 0.5 keV/µm in water were found at 100 MeV and 140 MeV, respectively. All the $LET_F$ profiles evaluated here showed an increase toward the depth of the Bragg peak followed by a plateau up to the maximum investigated depth.

Following the comparison with the MiniPIX-Timepix measurements, $LET_F$ was scored directly in the water phantom in 2 x 2 x 2 $mm^3$ voxels. The distribution of the $LET_F$ in the x-z plane was evaluated as well as the difference between the scored values for the collimated and uncollimated fields. The latter was calculated as $\langle LET_{F\_collimated} - LET_{F\_uncollimated} \rangle$ in each voxel. These results are displayed in **Figure 9**. The differences between the two cases in terms of $LET_D$ were also evaluated and shown in **Figure 10**.

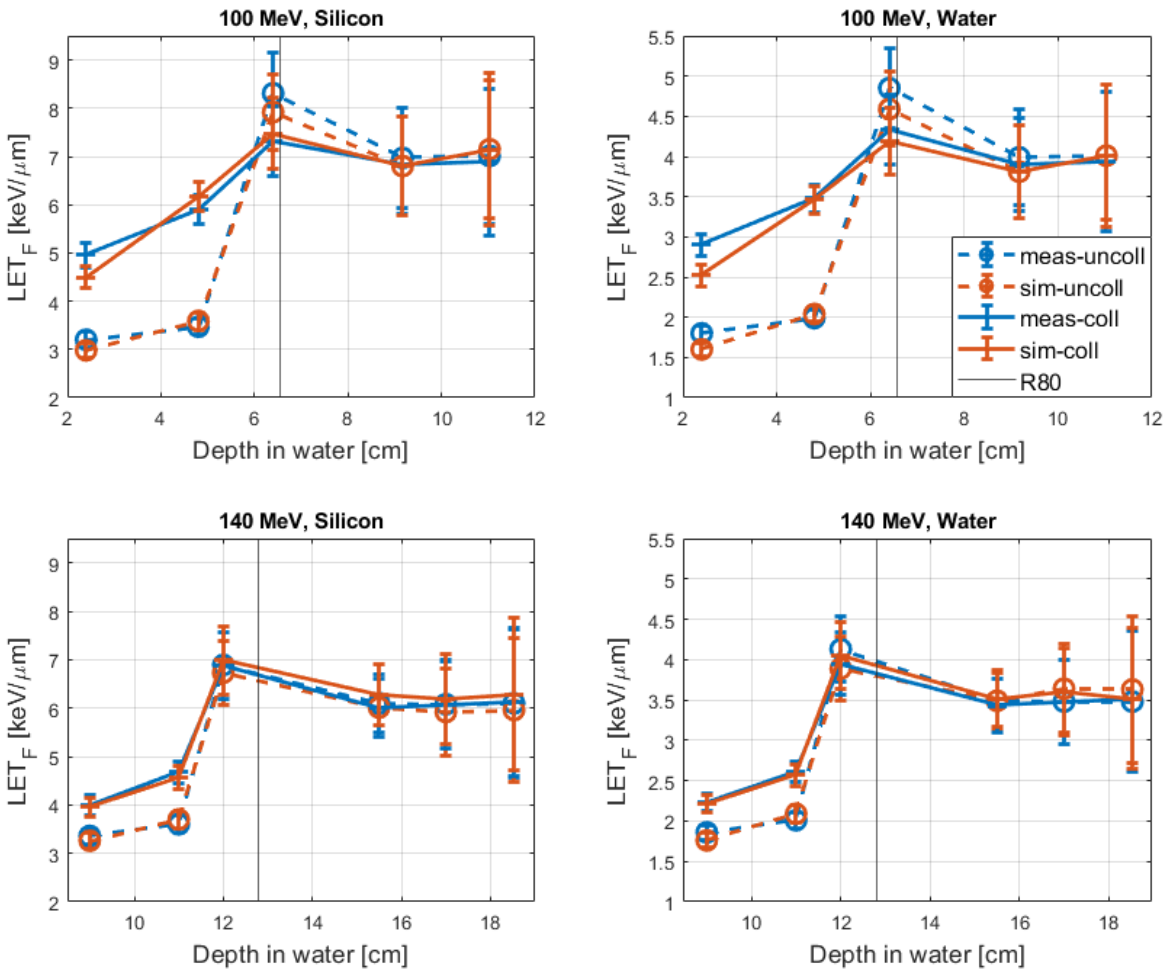


**Figure 8.** Measured and simulated $LET_F$ in silicon and water for 100 and 140 MeV proton beams, for collimated (solid lines) and uncollimated (dashed lines) fields, at 7.8 cm from the center of the field and at various depths in water. The range of protons ($R_{80}$) is indicated by a vertical line in each plot. Error bars represent the statistical uncertainty (k=1) and lines are to guide the eye.

Aperture-collimated fields were shown to increase $LET_F$ and $LET_D$ by a maximum of 3.5 keV/µm and 7 keV/µm at 100 MeV, respectively. These values dropped by about 43% at 140 MeV. The impact of the collimation was the highest close to the depth of the Bragg peak at 100 MeV, whereas at 140 MeV, a similar impact was also shown in the entrance region. Furthermore, the highest impact on the LET was observed primarily in low dose regions. For instance, at 100 MeV, an increase above 2 keV/µm in $LET_F$ relative to uncollimated fields was observed only in voxels receiving less than 20% of the maximum dose. The same increase in $LET_D$ was restricted to voxels

receiving less than 4% of the maximum dose. On the other hand, at 140 MeV, voxels exhibiting an increase above 1 keV/µm in $LET_F$ and $LET_D$ received less than 14% and 4% of the maximum dose, respectively.

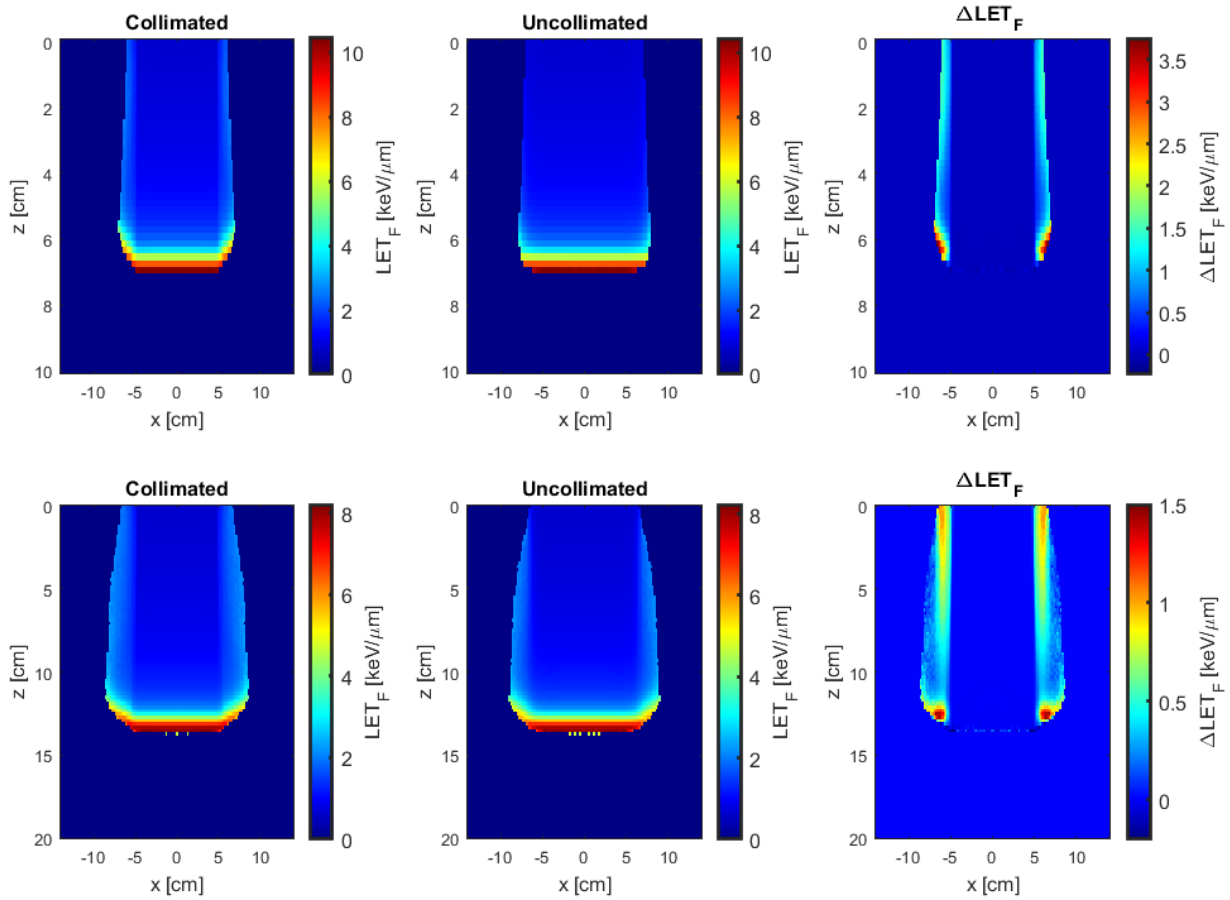


**Figure 9.** Simulated $LET_F$ distribution in the x-z plane of collimated, uncollimated and the difference between the two for 100 MeV (top) and 140 MeV (bottom). The displayed values are shown only for voxels in which the dose was higher than 0.1% of the maximum dose.

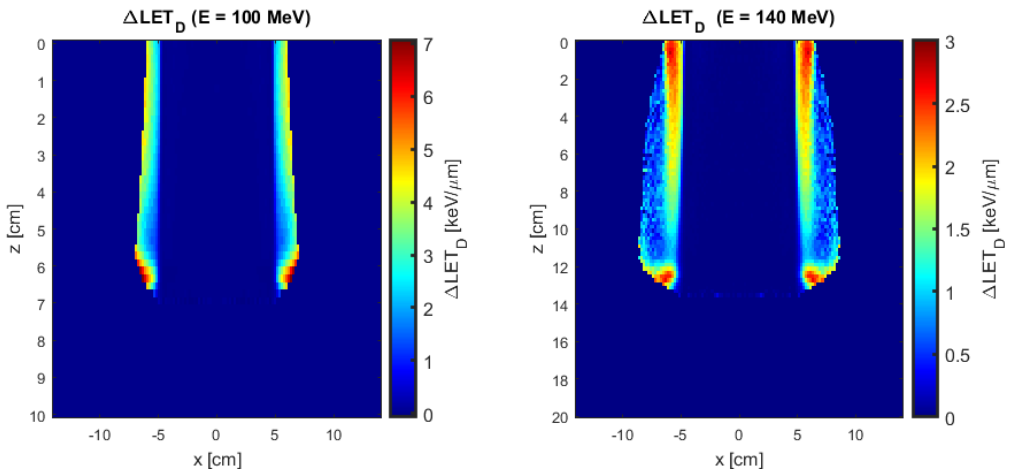


**Figure 10.** Same x-z distributions as Figure 9 but for $LET_D$ showing the difference between collimated and uncollimated fields for 100 MeV (left) and 140 MeV (right).

## 3.4. DNA damage

The absorbed dose and $LET_F$ in water in each voxel were then used to estimate the biological impact. The DNA damage was calculated using two LET-based models from the literature. Namely, the model developed by Kundrát *et al* (2020) was used to calculate the total DSB yield and DSB sites, while the model developed by Henthorn *et al* (2019) was used to calculate the yield of simple and complex DSB. Because of the significant dose reduction achieved by using the aperture, it was found that DSB yields and number of DSB sites were higher for uncollimated fields relative to the collimated ones. The absolute differences, denoted by Δ, are illustrated in **Figure 11** for 100 MeV and in **Figure 12** for 140 MeV. Interestingly, both DSB yields (simple and complex) and DSB sites were 1.5 times higher for 100 MeV compared to 140 MeV. Due to the increased $LET_F$ for collimated beams, the DSB yield per Gy per cell is higher for collimated fields, if the doses in each voxel are not taken into account (**Supp fig.** and **Supp fig. 3**).

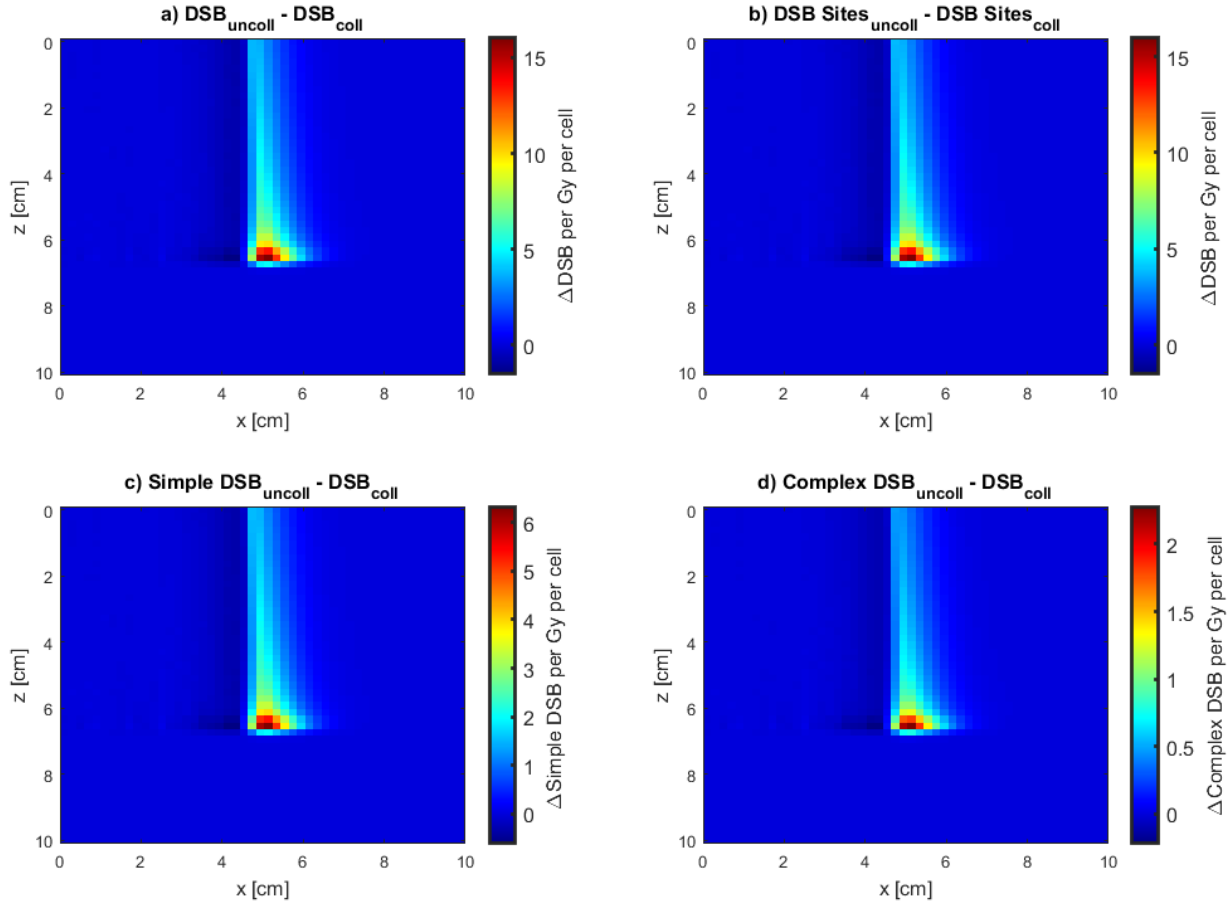


**Figure 11.** Differences in DNA damage between uncollimated and collimated fields at 100 MeV. Predictions based on the formulas of (Kundrát *et al* 2020) used to calculate the difference in total DSB yield (a) and total DSB sites (b). Predictions based on the model of (Henthorn *et al* 2019) used to calculate the difference in simple DSB (c) and complex DSB (d). Because the field is symmetrical, only positive x values are displayed. All calculations assume 6 Gbp of DNA and the values were normalized to the dose at the Bragg peak.

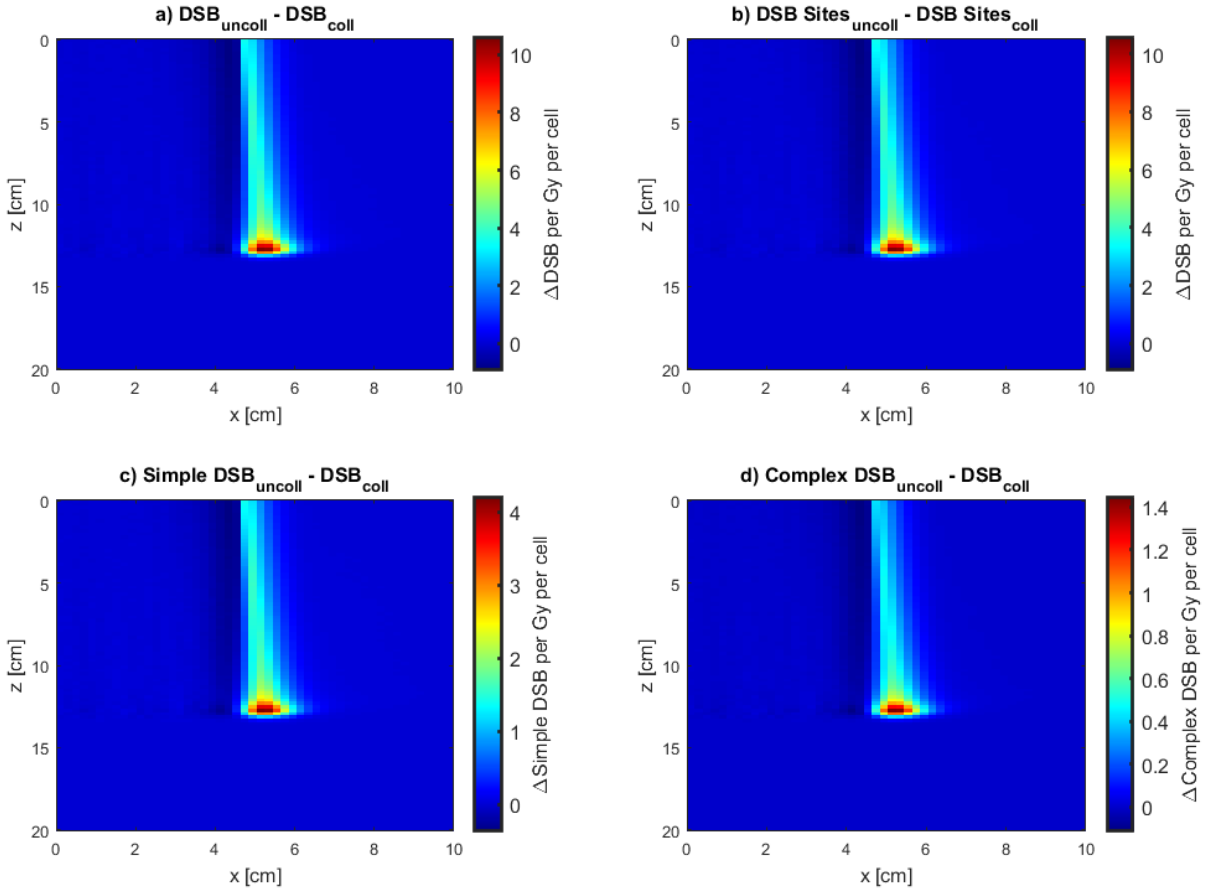


**Figure 12.** Differences in DNA damage between uncollimated and collimated fields at 140 MeV. Predictions based on the formulas of (Kundrát *et al* 2020) used to calculate the difference in total DSB yield (a) and total DSB sites (b). Predictions based on the model of (Henthorn *et al* 2019) used to calculate the difference in simple DSB (c) and complex DSB (d). Because the field is symmetrical, only positive x values are displayed. All calculations assume 6 Gbp of DNA and the values were normalized to the dose at the Bragg peak.

## 4. Discussion

MC simulations and measurements with a Timepix detector were used to characterize the dose in the lateral fall-off and out-of-field in collimated and uncollimated proton PBS. In this work, we also presented a methodology for calculating dose and proton $LET_F$ in water derived from measurements with a silicon-based MiniPIX-Timepix detector. Our findings confirmed that combining PBS with aperture resulted in a smaller penumbra and a sharper dose fall-off, which is in line with previous studies. Simulation results showed a dose reduction of up to 60% in the

lateral fall off when the aperture was used, and measurements showed an average reduction of 65% at larger distances from the field edge.

Analysis of the measured deposited energy spectra by protons revealed two prominent peaks at 1.9 and 3.9 MeV for the uncollimated field. On the contrary, protons in the collimated field presented a smaller peak centered between the two uncollimated deposited energy peaks. The measurements also showed that the majority of protons in the collimated field reached the sensor at larger angles when compared to the angular distribution of protons in the uncollimated field. These two observations point towards the fact that combining apertures with PBS blocked most of the air scattered protons, which retain their primary high energy, while the detected protons were mainly scattered with reduced energies.

Moreover, we found that using an aperture with PBS resulted in higher LET values in the lateral fall-off. MC simulations showed that the absolute $LET_F$ values increased by a maximum of 3.5 keV/µm relative to the uncollimated field, while $LET_D$ increased by a maximum of 7 keV/µm. The highest differences were observed at the lower beam energy and close to the depth of the Bragg peak. This trend was also supported by experimental results, which showed an increase of 1.5 keV/µm in $LET_F$ in water further away from the field edge. Although no comparison was made with uncollimated fields, Ueno *et al.* also showed through MC simulations that the $LET_D$ of collimator-scattered protons was several keV/µm higher than that of unscattered ones, in a set of investigated positions (Ueno *et al* 2019). The reported increase is also in agreement with the results found in this work in terms of $LET_D$, although a direct comparison cannot be made given the differences in the irradiated fields, scored quantities and positions. Furthermore, in the same study, an increase in $LET_D$ of collimator-scattered protons (relative to unscattered) higher than 1 keV/µm was observed only in voxels receiving less than 4% of the prescription dose. In this work, a slightly higher increase of 2 keV/µm in $LET_D$ (relative to uncollimated fields) was observed in voxels receiving 4% of the maximum dose, while the highest increase in $LET_D$ was found in voxels receiving less than 0.5% of the maximum dose. Essentially, both studies confirm that the highest increase in LET occurs only in low-dose regions. To the best of our knowledge, the increase in LET

caused by combining PBS with apertures has never been demonstrated experimentally and compared with uncollimated cases.

Overall, the impact of collimation on the lateral fall-off (i.e. lower dose, higher LET) was shown to be more significant at the lower beam energy. As it was shown in (Safai *et al* 2008), the contribution of the scattering in air to the total spread in water, was higher for lower beam energies. This contribution decreases with increasing beam energy, where the effect of scattering in the target becomes more important. This is also in agreement with another study, in which the authors found that the use of aperture was mainly beneficial for treating shallow targets in terms of penumbra reduction (Maes *et al* 2019).

Measured and simulated doses revealed similar trends, however, their discrepancy could be attributed to a number of factors. Firstly, measurements in the sensitive volume were compared to simulations in which the dose was directly scored in the water without the influence of the detector and its holder. Secondly, the target size was slightly different since the simulated dose was scored in 2 x 2 x 2 $mm^3$ voxels, while the measured dose was averaged over a sensitive volume of 14 x 14 x 0.5 $mm^3$ of silicon. Considering the heterogeneity of the radiation field in the measurement positions, small discrepancies between the measured and simulated doses could be expected. Even though the different scoring materials and slightly varying volumes can be considered a limitation of the study design, we believe this impact is small and preferred to generate 2D dose maps for scoring appropriate quantities required for prediction of DSBs.

Other important factors in the calculation of the measured dose in water are particle identification and dead-time correction. One limitation of the former is that all the heavier ions were grouped into one class using the current DPE algorithm. However, the contribution of the heavy recoil ions to the total number of detected events was less than 3% for all the measurements. In another study, MC simulations showed that the contribution of secondary ions to the total dose in a water phantom, was less than 1% in the entrance and plateau region of a 160 MeV beam, and was dominated by alpha particles (Grassberger and Paganetti 2011). Therefore, the impact of heavy ion identification using the MiniPIX-Timepix on the calculation of total dose can be considered negligible in this work. However, their impact on the biological

effects might be non-negligible and is a subject for future studies. As more validation and testing of the DPE is currently being performed, it is expected that a more precise particle identification will be achieved. The dead-time correction can also be circumvented by switching to Timepix3 detectors, which have nearly no dead-time. Consequently, they are better suited for measurements at clinical beam intensities. Future work will focus on improving the calculation and conversion of dose and LET measured by silicon-based Timepix detectors.

Proton $LET_F$ measured by the single-layer Timepix detector was validated in another work using mono-energetic proton beams and MC simulations (Nabha *et al* 2022). An ad hoc extension was needed in this work to account for stopping protons. The results were promising, given that a maximum difference of 14% was found between measured and simulated $LET_F$ in water at the same positions. Nonetheless, a systematic validation of this extension with mono-energetic low-energy beams incident at different angles will be performed to confirm the validity of our method. Although it can be argued that $LET_D$ is more clinically relevant than $LET_F$, the choice of calculating and comparing the measured and simulated $LET_F$ in this work was based on the fact that different MC studies showed that $LET_F$ is less sensitive to simulation parameters compared to $LET_D$ (Granville and Sawakuchi 2015, Cortés-Giraldo and Carabe 2015). Moreover, since we are interested in the impact of the aperture, which primarily affects the dose and LET distributions in the dose plateau region and proximal to the Bragg peak, it was also recommended by (Guan *et al* 2015) to score $LET_F$ instead of $LET_D$ in this region due to the strong dependence of the latter on the upper limit of a tracking step length, also known as step size. Lastly, the DNA damage models used in this work were also $LET_F$ dependent. It should be noted that $LET_F$ is sometimes referred to as $LET_t$ due to historical reasons (Wilkens and Oelfke 2003, Guan *et al* 2015).

Finally, albeit higher LET values were found in the lateral fall-off of collimated fields, the predicted DNA damage remained lower than in the uncollimated cases owing to the large dose reduction. Uncollimated fields induced a maximum increase in absolute DSB yields of 16 ($Gy^{-1}$) and a maximum increase in complex DSB up to 2 ($Gy^{-1}$), at 100 MeV. The absolute differences in simple and complex DSB yields, as well as DSB sites were 1.5 times higher for 100 MeV compared to 140 MeV.

The choice of DNA damage as a biological endpoint was supported by the fact that the primary region of interest concerns normal tissues where colony survival might not be an adequate endpoint. For this reason, prediction of DSB based on dose and LET might give better insight on potential DNA damage and complexity. Since track structure simulations can be cumbersome, the formulas used in this work, as stated by the authors, can be extrapolated to macroscopic targets. It should be noted that track structure parameters such as the chemistry and physics models, damage thresholds, chemical stage length and target geometry can have a large effect on the simulation results (Wu *et al* 2020, Zhu *et al* 2020). Although the track structure codes and parameters were different, both *in silico* models used for the prediction of DNA damage showed a similar pattern in terms of DSB yield and complexity despite the differences in absolute yield. Ideally, a multi-scale approach that also accounts for the DNA repair, the impact at the cellular and tissue level leading to normal tissue complexity probability (NTCP) would better represent the clinical outcome. Consequently, despite the reduction of DNA damage observed in collimated fields, additional investigations are needed to confirm the overall benefits on clinical outcome.

The rationale for using simplified proton fields consisting of single energy layers delivered in square fields was to establish a characterization of the radiation fields, based on first principles, and to use this information to assess DNA damage which can be related to the impact on clinical outcome. The method presented in this work can be used in future work to explore more complex clinically relevant scenarios where the impact of collimation on dose and LET distributions might be very different.

## 5. Conclusion

Dosimetric and biophysical characterization of the uncollimated and aperture-collimated proton PBS fields were presented in this work. The compact MiniPIX-Timepix detector was shown to be a suitable tool for measuring particle-specific absorbed dose and LET in mixed radiation fields. It was found through simulations that the absolute protons $LET_F$ values in collimated fields increased by a maximum of 3.5 keV/µm relative to the uncollimated field, while proton $LET_D$ increased by a maximum of 7 keV/µm. The highest impact was found at the lateral field edges of collimated beams and extending up to a few cm. Nevertheless, using published *in silico* models,

the DNA damage was found to be higher in the lateral fall-off of uncollimated fields. Generally, the biophysical impact of using the aperture was more pronounced at 100 MeV compared to 140 MeV. Although the overall impact on DNA damage was shown to be favorable in collimated fields owing to the dose reduction effect, care should be taken when organs at risk are present in lateral dose fall-off regions.

## References


Bäumer C, Geismar D, Koska B, Kramer P H, Lambert J, Lemke M, Plaude S, Pschichholz L, Qamhiyeh S, Schiemann A, Timmermann B and Vermeren X 2017 Comprehensive clinical commissioning and validation of the RayStation treatment planning system for proton therapy with active scanning and passive treatment techniques *Phys. Medica* **43** 15–24

Bäumer C, Janson M, Timmermann B and Wulff J 2018 Collimated proton pencil-beam scanning for superficial targets: impact of the order of range shifter and aperture *Phys. Med. Biol.* **63** Online: https://pubmed.ncbi.nlm.nih.gov/29553047/

Bäumer C, Koska B, Lambert J, Timmermann B, Mertens T and Talla P T 2015 Evaluation of detectors for acquisition of pristine depth-dose curves in pencil beam scanning *J. Appl. Clin. Med. Phys.* **16** 151–63 Online: https://pubmed.ncbi.nlm.nih.gov/26699567/

Bäumer C, Plaude S, Khalil D A, Geismar D, Kramer P H, Kröninger K, Nitsch C, Wulff J and Timmermann B 2021 Clinical Implementation of Proton Therapy Using Pencil-Beam Scanning Delivery Combined With Static Apertures *Front. Oncol.* **11** 1377

Berger M J, Coursey J S, Zucker M A and Chang J 2005 ESTAR, PSTAR, and ASTAR: Computer Programs for Calculating Stopping-Power and Range Tables for Electrons, Protons, and Helium Ions (version 1.2.3) *Natl. Inst. Stand. Technol.* Online: https://www.nist.gov/pml/stopping-power-and-range-tables-electrons-protons-and-helium-ions-version-history

Campbell M, Heijne E, Holý T, Idárraga J, Jakůbek J, Lebel C, Leroy C, Llopart X, Pospíšil S, Tlustos L and Vykydal Z 2008 Study of the charge sharing in a silicon pixel detector by means of α-particles interacting with a Medipix2 device *Nucl. Instruments Methods Phys. Res. Sect. A Accel. Spectrometers, Detect. Assoc. Equip.* **591** 38–41

Charlwood F C, Aitkenhead A H and MacKay R I 2016 A Monte Carlo study on the collimation of pencil beam scanning proton therapy beams *Med. Phys.* **43** 1462–72

Cortés-Giraldo M A and Carabe A 2015 A critical study of different Monte Carlo scoring methods of dose average linear-energy-transfer maps calculated in voxelized geometries irradiated with clinical proton beams *Phys. Med. Biol.* **60** 2645–69 Online: https://pubmed.ncbi.nlm.nih.gov/25768028/

Durante M and Paganetti H 2016 Nuclear physics in particle therapy: a review *Reports Prog. Phys.* **79** 096702 Online: https://iopscience.iop.org/article/10.1088/0034-4885/79/9/096702

Faddegon B, Ramos-Méndez J, Schuemann J, McNamara A, Shin J, Perl J and Paganetti H 2020 The TOPAS tool for particle simulation, a Monte Carlo simulation tool for physics, biology and clinical research *Phys. Medica* **72** 114–21

Granja C, Jakubek J, Köster U, Platkevic M and Pospisil S 2011 Response of the pixel detector Timepix to heavy ions *Nucl. Instruments Methods Phys. Res. Sect. A Accel. Spectrometers, Detect. Assoc. Equip.* **633** 198–202

Granja C, Jakubek J, Polansky S, Zach V, Krist P, Chvatil D, Stursa J, Sommer M, Ploc O, Kodaira S and Martisikova M 2018a Resolving power of pixel detector Timepix for wide-range electron, proton and ion detection *Nucl. Instruments Methods Phys. Res. Sect. A Accel. Spectrometers, Detect. Assoc. Equip.* **908**

Granja C, Krist P, Chvatil D, Solc J, Pospisil S, Jakubek J and Opalka L 2013 Energy loss and online directional track visualization of fast electrons with the pixel detector Timepix *Radiat. Meas.* **59** 245–61

Granja C, Kudela K, Jakubek J, Krist P, Chvatil D, Stursa J and Polansky S 2018b Directional detection of charged particles and cosmic rays with the miniaturized radiation camera MiniPIX Timepix *Nucl. Instruments Methods Phys. Res. Sect. A Accel. Spectrometers, Detect. Assoc. Equip.* **911** 142–52 Online: https://doi.org/10.1016/j.nima.2018.09.140

Granville D A and Sawakuchi G O 2015 Comparison of linear energy transfer scoring techniques in Monte Carlo simulations of proton beams *Phys. Med. Biol.*

Grassberger C and Paganetti H 2011 Elevated LET components in clinical proton beams *Phys. Med. Biol.* **56** 6677 Online: https://iopscience.iop.org/article/10.1088/0031-9155/56/20/011

Guan F, Peeler C, Bronk L, Geng C, Taleei R, Randeniya S, Ge S, Mirkovic D, Grosshans D, Mohan R and Titt U 2015 Analysis of the track- and dose-averaged LET and LET spectra in proton therapy using the geant4 Monte Carlo code *Med. Phys.* **42** 6234–47 Online: https://onlinelibrary.wiley.com/doi/full/10.1118/1.4932217

Henthorn N T, Warmenhoven J W, Sotiropoulos M, Aitkenhead A H, Smith E A K, Ingram S P, Kirkby N F, Chadwick A L, Burnet N G, MacKay R I, Kirkby K J and Merchant M J 2019 Clinically relevant nanodosimetric simulation of DNA damage complexity from photons and protons *RSC Adv.* **9** 6845–58 Online: https://pubs.rsc.org/en/content/articlehtml/2019/ra/c8ra10168j

Hubbell J H and Seltzer S M 1996 NIST: X-Ray Mass Attenuation Coefficients *Phys. Ref. Data*

Hyer D E, Hill P M, Wang D, Smith B R and Flynn R T 2014 A dynamic collimation system for penumbra reduction in spot-scanning proton therapy: Proof of concept *Med. Phys.* **41** 091701 Online: https://onlinelibrary.wiley.com/doi/full/10.1118/1.4837155

Knopf A C and Lomax A 2013 In vivo proton range verification: a review *Phys. Med. Biol.* **58** 131–60 Online: https://pubmed.ncbi.nlm.nih.gov/23863203/

Kundrát P, Friedland W, Becker J, Eidemüller M, Ottolenghi A and Baiocco G 2020 Analytical formulas representing track-structure simulations on DNA damage induced by protons and light ions at radiotherapy-relevant energies *Sci. Reports 2020 101* **10** 1–11 Online: https://www.nature.com/articles/s41598-020-72857-z

Llopart X, Ballabriga R, Campbell M, Tlustos L and Wong W 2007 Timepix, a 65k programmable pixel readout chip for arrival time, energy and/or photon counting measurements *Nucl. Instruments Methods Phys. Res. Sect. A Accel. Spectrometers, Detect. Assoc. Equip.* **581** 485–94

Lühr A, von Neubeck C, Krause M and Troost E G C 2018 Relative biological effectiveness in proton beam therapy – Current knowledge and future challenges *Clin. Transl. Radiat.*

*Oncol.* **9** 35 Online: /pmc/articles/PMC5862688/

Maes D, Regmi R, Taddei P, Bloch C, Bowen S, Nevitt A, Leuro E, Wong T, Rosenfeld A and Saini J 2019 Parametric characterization of penumbra reduction for aperture-collimated pencil beam scanning (PBS) proton therapy *Biomed. Phys. Eng. Express* **5** 035002 Online: https://iopscience.iop.org/article/10.1088/2057-1976/ab0953

Marek L, Granja C and Jakubek J 2023 Data Processing Engine for Timepix Detectors (in preparation) *Nucl. Instruments Methods Phys. Res. Sect. A Accel. Spectrometers, Detect. Assoc. Equip.*

Moignier A, Gelover E, Wang D, Flynn R T, Kirk M L, Lin L, Solberg T D, Lin A and Hyer D 2015 Benefits of Collimation in Head and Neck Cancers Treated With Spot Scanning Proton Therapy *Int. J. Radiat. Oncol.* **93** E580 Online: http://www.redjournal.org/article/S0360301615027704/fulltext

Nabha R, Van Hoey O, Granja C, Parisi A, De Saint-Hubert M, Struelens L, Oancea C, Sterpin E, Zach V, Stursa J, Rucinski A, Gajewski J, Stasica P and Vanhavere F 2022 A novel method to assess the incident angle and the LET of protons using a compact single-layer Timepix detector *Radiat. Phys. Chem.* **199** 110349

Nelson N P, Culberson W S, Hyer D E, Geoghegan T J, Patwardhan K A, Smith B R, Flynn R T, Yu J, Rana S, Gutiérrez A N and Hill P M 2021 Development and validation of the Dynamic Collimation Monte Carlo simulation package for pencil beam scanning proton therapy. *Med. Phys.* **48** 3172–85 Online: https://europepmc.org/articles/PMC8273151

Paganetti H, Blakely E, Carabe-Fernandez A, Carlson D J, Das I J, Dong L, Grosshans D, Held K D, Mohan R, Moiseenko V, Niemierko A, Stewart R D and Willers H 2019 Report of the AAPM TG-256 on the relative biological effectiveness of proton beams in radiation therapy *Med. Phys.* **46** e53–78

Paganetti H, Niemierko A, Ancukiewicz M, Gerweck L E, Goitein M, Loeffler J S and Suit H D 2002 Relative biological effectiveness (RBE) values for proton beam therapy *Int. J. Radiat. Oncol.* **53** 407–21

Parisi A, Olko P, Swakoń J, Horwacik T, Jabłoński H, Malinowski L, Nowak T, Struelens L and Vanhavere F 2022 Microdosimetric characterization of a clinical proton therapy beam: comparison between simulated lineal energy distributions in spherical water targets and experimental measurements with a silicon detector *Phys. Med. Biol.* **67** 015006 Online: https://iopscience.iop.org/article/10.1088/1361-6560/ac4563

Perl J, Shin J, Schümann J, Faddegon B and Paganetti H 2012 TOPAS: An innovative proton Monte Carlo platform for research and clinical applications *Med. Phys.* **39** 6818–37 Online: https://pubmed.ncbi.nlm.nih.gov/23127075/

Safai S, Bortfeld T and Engelsman M 2008 Comparison between the lateral penumbra of a collimated double-scattered beam and uncollimated scanning beam in proton radiotherapy *Phys. Med. Biol.* **53** 1729–50 Online: https://pubmed.ncbi.nlm.nih.gov/18367800/

De Saint-Hubert M, Verbeek N, Bäumer C, Esser J, Wulff J, Nabha R, Van Hoey O, Dabin J, Stuckmann F, Vasi F, Radonic S, Boissonnat G, Schneider U, Rodriguez M, Timmermann B, Thierry-Chef I and Brualla L 2022 Validation of a Monte Carlo Framework for Out-of-Field Dose Calculations in Proton Therapy *Front. Oncol.* **12** 2452

Schneider U, Agosteo S, Pedroni E and Besserer J 2002 Secondary neutron dose during proton therapy using spot scanning. *Int. J. Radiat. Oncol. Biol. Phys.* **53** 244–51 Online:

http://www.ncbi.nlm.nih.gov/pubmed/12007965
Stasica P, Baran J, Granja C, Krah N, Korcyl G, Oancea C, Pawlik-Niedźwiecka M, Niedźwiecki S, Rydygier M, Schiavi A, Rucinski A and Gajewski J 2020 A Simple Approach for Experimental Characterization and Validation of Proton Pencil Beam Profiles *Front. Phys.* **8** 346 Online: https://www.frontiersin.org/articles/10.3389/fphy.2020.00346/full
Tattenberg S, Madden T M, Bortfeld T, Parodi K and Verburg J 2022 Range uncertainty reductions in proton therapy may lead to the feasibility of novel beam arrangements which improve organ-at-risk sparing *Med. Phys.* **49** 4693–704 Online: https://onlinelibrary.wiley.com/doi/full/10.1002/mp.15644
Ueno K, Matsuura T, Hirayama S, Takao S, Ueda H, Matsuo Y, Yoshimura T and Umegaki K 2019 Physical and biological impacts of collimator-scattered protons in spot-scanning proton therapy *J. Appl. Clin. Med. Phys.* **20** 48–57 Online: https://pubmed.ncbi.nlm.nih.gov/31237090/
Verbeek N, Wulff J, Bäumer C, Smyczek S, Timmermann B and Brualla L 2021 Single pencil beam benchmark of a module for Monte Carlo simulation of proton transport in the PENELOPE code *Med. Phys.* **48** 456–76 Online: https://onlinelibrary.wiley.com/doi/full/10.1002/mp.14598
Vitti E T and Parsons J L 2019 The Radiobiological Effects of Proton Beam Therapy: Impact on DNA Damage and Repair *Cancers (Basel).* **11** Online: /pmc/articles/PMC6679138/
Wilkens J J and Oelfke U 2003 Analytical linear energy transfer calculations for proton therapy *Med. Phys.* **30** 806–15 Online: https://onlinelibrary.wiley.com/doi/full/10.1118/1.1567852
Winterhalter C, Lomax A, Oxley D, Weber D C and Safai S 2018 A study of lateral fall-off (penumbra) optimisation for pencil beam scanning (PBS) proton therapy *Phys. Med. Biol.* **63** Online: https://pubmed.ncbi.nlm.nih.gov/29324441/
Wu J, Xie Y, Wang L and Wang Y 2020 Monte Carlo simulations of energy deposition and DNA damage using TOPAS-nBio *Phys. Med. Biol.* **65** 225007 Online: https://iopscience.iop.org/article/10.1088/1361-6560/abbb73
Zhu H, Mcnamara A L, Ramos-Mendez J, Mcmahon S J, Henthorn N T, Faddegon B, Held K D, Perl J, Li J, Paganetti H and Schuemann J 2020 A parameter sensitivity study for simulating DNA damage after proton irradiation using TOPAS-nBio *Phys. Med. Biol.* **65** Online: https://pubmed.ncbi.nlm.nih.gov/32101803/

# 6. Supplementary material

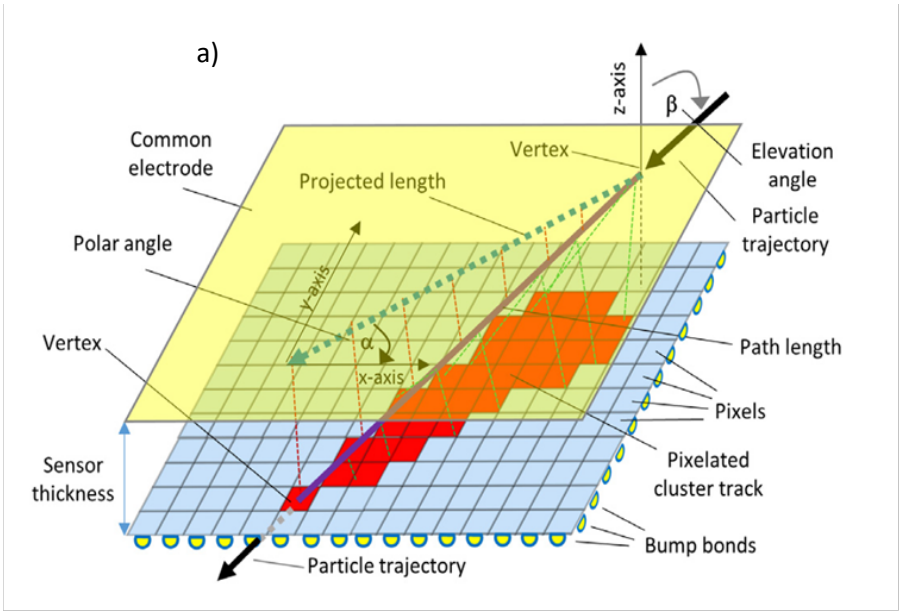


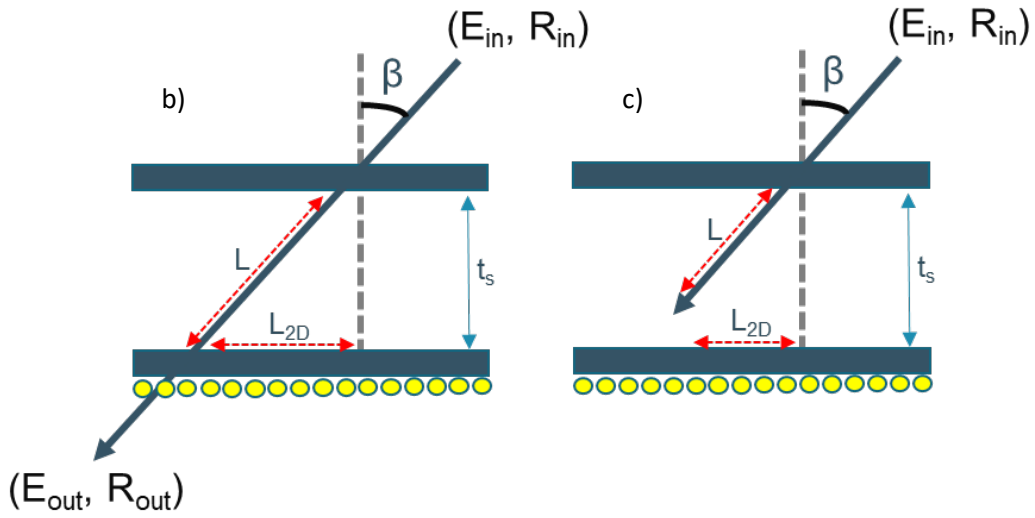


**Supp fig. 1.** Particle tracking in Timepix detector (a) illustrating the main components of the sensor and the particle's path across the sensitive volume, reprinted from (Granja et al 2018b). Schematic representation of a crossing particle (b) and a stopping particle (c).

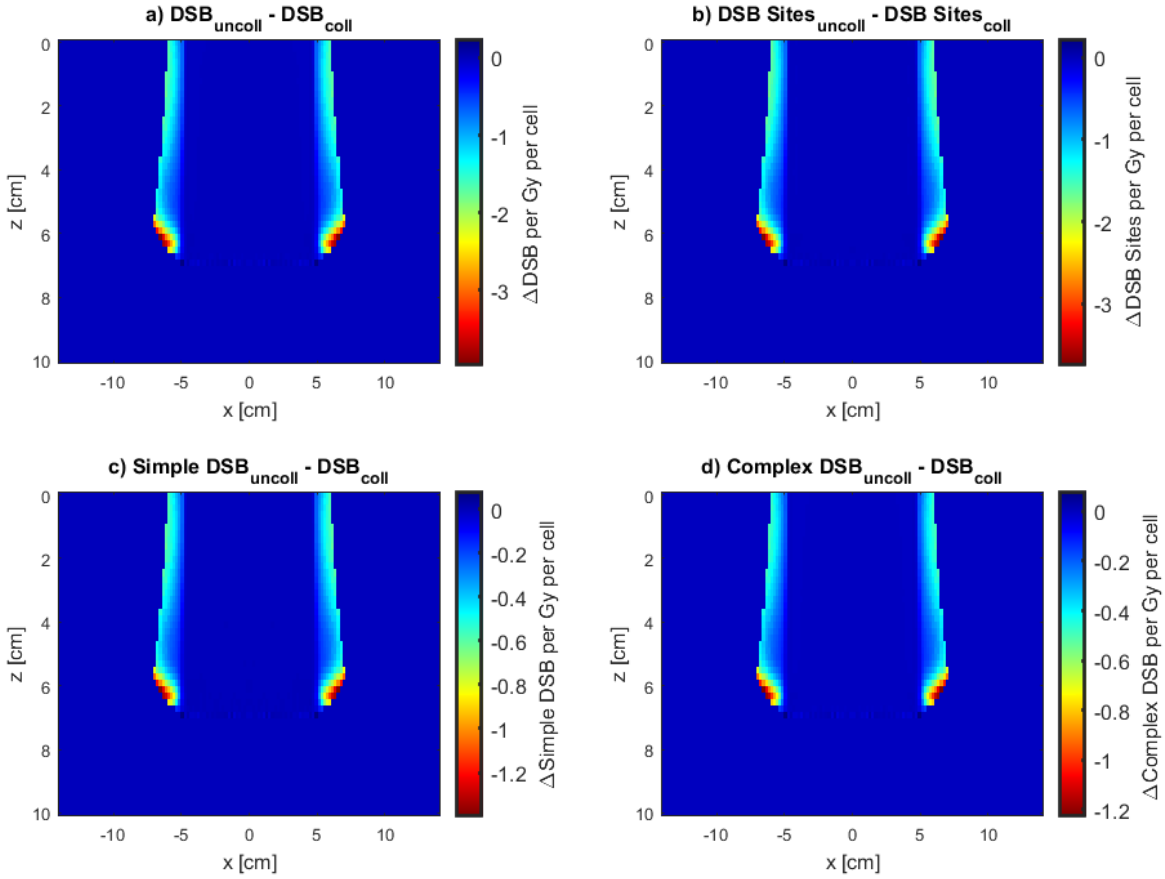


**Supp fig. 2.** The same as Figure 11 without taking into account the dose per voxel and only the simulated $LET_F$.

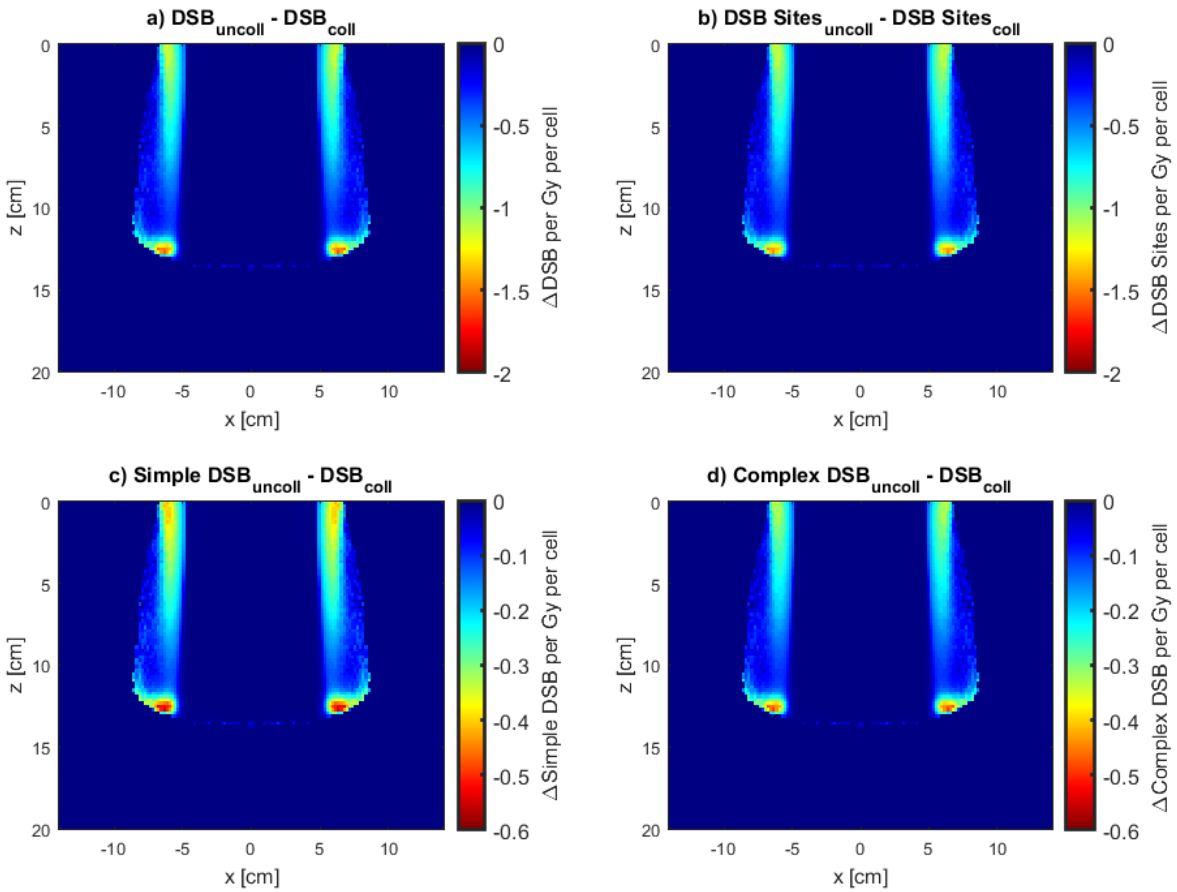


**Supp fig. 3.** The same as Figure 12 without taking into account the dose per voxel and only the simulated $LET_F$.